Achieving Product Control in Furfural Hydrogenation Using Intermetallic Catalysts

Charles J. Ward[1,2], Minda Chen[3], Andrew Lamkins[1,2], Claudio Ordonez[1], Rong Sun[1], Puranjan Chatterjee[1,2], Minghui Niu[1], Ruoyu Cui[1], Da-Jiang Liu[2*], and Wenyu Huang[1,2*]

[1]Department of Chemistry, Iowa State University, Ames, IA 50011, United States

[2]Ames National Laboratory, US Department of Energy, Ames, IA 50011, United States

[3]Materials and Structural Analysis Division, Thermo Fisher Scientific, Hillsboro, OR, 97124, United States

*Corresponding author. E-mail: whuang@iastate.edu; dajiang@ameslab.gov

ABSTRACT: Intermetallic nanoparticles (iNPs) have garnered much attention as effective catalysts, but the impact of tuning surface properties to induce steric effects is relatively unexplored. Here, we report on the strategy of governing steric hindrance in bimetallic catalysts as a method to alter product selectivity in furfural hydrogenation using Rh-based iNPs by varying the size of the secondary metal atoms. RhGa, RhIn, and RhBi nanoparticles were synthesized within confined mesoporous silica wells (MSWs) and assessed for the vapor-phase hydrogenation of furfural. RhGa and RhIn iNPs enable product control with an enhanced selectivity to furan and furfuryl alcohol (> 90 %) compared to the monometallic Rh@MSW. Adding Bi to Rh inhibits the transformation of furfural almost entirely. In-situ diffuse reflectance infrared Fourier transform spectroscopy studies and density functional theory-based machine-learning accelerated molecular dynamics simulations reveal that the secondary metal's identity strongly impacts the preferred furfural adsorption mode on the active sites, leading to the observed catalysis control. The mesoporous silica shell of the RhM@MSW catalyst provides protection against NP aggregation under reaction and regeneration conditions, as supported by good stability during recycling studies.

KEYWORDS: Intermetallic compounds, heterogenous catalysis, intermetallic nanoparticles, diffuse reflectance infrared Fourier transform spectroscopy, DRIFTS, selective hydrogenation

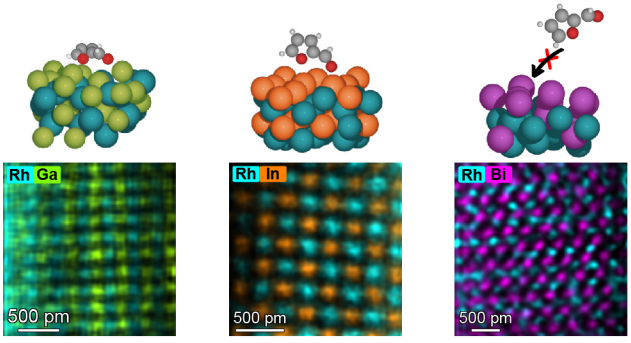

TOC graphic. Depiction of different furfural adsorption modes on intermetallic compound surfaces, leading to different major products formed.

1. Introduction

Intermetallic compounds (IMCs) are a type of ordered alloy with defined stoichiometry and crystal structure. Intermetallic nanoparticles (iNPs) have been recognized as effective catalysts with excellent activity, selectivity, and durability in various reactions.[1,2] The addition of a secondary metal enables control over the catalyst's electronic and atomic level structures, leading to electronic, geometric, steric, and ordering effects that greatly influence their catalytic performance.[3] The impact of modifying the electronic and geometric properties of active metals by forming intermetallic compounds has been widely explored.[4–7] In contrast, utilizing the well-defined iNP surface to create sterically hindered active sites remains under-explored.

The limited examples of designing an iNP surface to restrict access to the active sites indicate that it is a viable strategy for controlling selectivity. Komatsu et al. described a "molecular recognition" capability in the hydrogenation of nitroarenes using RhM/SiO_2, where they observed a preferential nitro group adsorption on the more sterically hindered Rh.[8] Komatsu further explored this behavior in the hydrogenation of dienes to monoenes. It was shown that for intermetallic compositions with larger secondary metals, such as Sn or Bi, adsorption of the inner C=C bond was inhibited, leading to the selective hydrogenation of the terminal C=C bond and preventing overhydrogenation to alkanes.[9] This surface-tuning strategy could be especially effective in more complex reactions that include multiple reaction pathways and possible products such as the hydrogenation of furfural.

With the growing economic and environmental demand to replace nonrenewable feedstocks in the chemical industry, the conversion of biomass to generate valuable fine chemicals is receiving increased attention.[10–12] The conversion of furfural, a biomass-derived platform chemical, has received much interest in this regard as it is used to produce numerous downstream chemicals, such as furan, furfuryl alcohol (FOL), tetrahydrofuran (THF), and 2-methylfuran (2-MF) which are then used in various products including resins, adhesives, solvents, and biofuels.[13–15] Furfural is primarily obtained from the hydrolysis and dehydration of agricultural waste-based sugars making it a sustainable platform compound without relying on food or fuel sources.

Transition metal catalysts, including Cu, Ni, Co, Pt, Pd, and Rh, have been explored for the conversion of furfural.[16–26] Many of the reported non-noble metal catalysts suffer from coking, require harsh conditions to achieve high conversions, and deactivate rapidly at high temperatures

due to sintering.[27–29] Noble metal-based catalysts, with enhanced hydrogenation abilities, have superior activity compared to non-noble metals but typically suffer from poor selectivity due to the reaction complexity and number of possible pathways, as displayed in Scheme 1. Previous studies have explored manipulating this selectivity and found it to be sensitive to many factors, including catalyst composition, catalyst support, active site size and morphology, and reaction conditions. Somorjai et al. demonstrated changing selectivity towards furfuryl alcohol and furan dependent on the size and shape of Pt NPs.[30] The effect of Pt NP size was further explored by Kyriakou and coworkers, who also investigated the impact of solvent choice on reaction activity and selectivity towards FOL.[31] Chen et al. reported tuning atomic ratios in Cu-Fe catalysts and reaction temperatures to produce FOL or 2-MF selectively.[32] While some tunability was achieved, overall selectivity remained low (<50% 2-MF). MIL-101 was used as an acidic support to increase the selectivity towards cyclopentanone using Ru-based catalysts in the transformation of furfural by Li and co-workers.[33] Even with the aforementioned examples, designing catalytic systems capable of effectively targeting multiple major products using a broadly applicable strategy remains challenging.

Achieving product control with a high degree of selectivity is highly desirable. In our previous work, PtSn, PtZn, and PtPb intermetallic catalysts exhibited high selectivity (>97% for PtSn) to furfuryl alcohol (FOL) and significantly improved activity compared to monometallic Pt.[34] This enhanced activity and selectivity towards FOL was attributed to furfural having a different adsorption configuration on the PtSn and Pt catalyst as suggested by DFT calculations. Similar results were observed using a Ni-Sn IMC system by Wei and co-workers, where increasing the secondary metal content switched the selectivity from tetrahydrofurfuryl alcohol to furfuryl alcohol with the Sn isolating the Ni sites and limiting the furan ring interaction with the active sites.[35] This apparent correlation between adsorption geometry and reaction selectivity makes furfural hydrogenation an ideal reaction to display the effectiveness of IMC-induced steric effects. This study aims to further explore and apply the characteristics of iNP catalysts, with a focus on steric effects, for the hydrogenation of furfural with the goal of achieving tunable product control while establishing a blueprint for future catalyst design. We detail an effective method of directing the reaction pathway of furfural hydrogenation with high selectivity by changing the inert metal component of RhM (M =Ga, In, Bi) iNPs and introducing surface steric effects. Vapor-phase hydrogenation of furfural resulted in highly selective production of furan over RhGa@MSWs,

FOL for RhIn@MSWs, and a sharply diminished activity for RhBi@MSW. In-situ diffuse reflectance infrared Fourier transform spectroscopy (DRIFTS) experiments and DFT-based machine learning (ML) accelerated molecular dynamics (MD) simulations were used to link the observed product control to the furfural adsorption configuration. Our results display the ability to alter reaction pathways by controlling the identity of the secondary metal in iNP catalysts. The nanoparticles are encapsulated in well-defined mesoporous silica wells (MSWs) to prevent sintering.[36–38] Catalyst regeneration and recycling tests demonstrated the stability of the RhM@MSW due to the unique synthesis strategy.

2. Results and Discussion

2.1 Synthesis and Characterization

Rh-based iNPs are encapsulated and confined between a solid silica core and a mesoporous silica shell with aligned channels, mimicking mesoporous wells (MSWs). The MSWs act as isolated nano-reactors and inhibit particle sintering during high-temperature treatments and catalytic reactions. The confined Rh nanoparticles remain accessible to metal precursors and small organic molecules via the channels in MSW.[18] This allows the addition of a secondary metal into the Rh@MSW to form the corresponding intermetallic compound nanoparticles (iNPs) and the furfural to reach the catalyst surface and interact with the active sites. An illustration of the synthesis process is summarized in Scheme 1, with transmission electron microscopy (TEM) images of the Rh NPs and the monodisperse spherical silica cores provided in Figures S1 and S2.

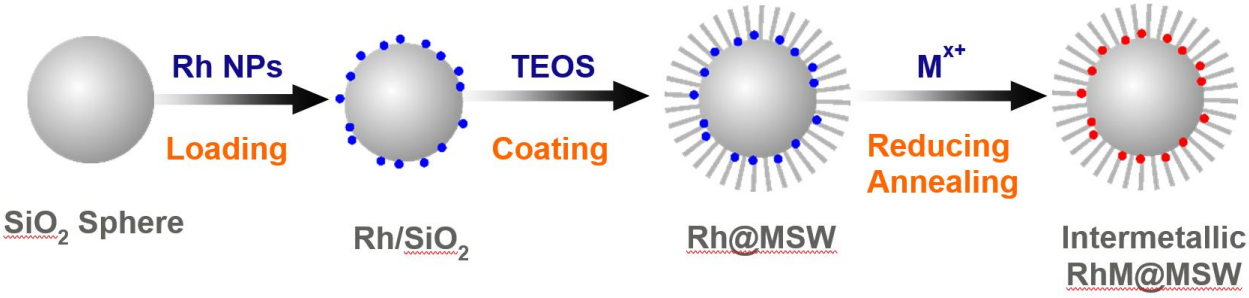

Scheme 1. Schematic synthesis procedure for RhM@MSWs showing the Rh decoration of the functionalized silica spheres followed by the mesoporous silica shell growth and the introduction and reduction of the secondary metals to form the intermetallic nanoparticles confined within the mesoporous silica wells.

The secondary metals (Ga, In, and Bi) were deliberately chosen to study the steric effect on the catalytic property of Rh. Based on prior reports, Bi (1.8 Å) was selected to be the largest of the secondary metals.[8,9] Ga (1.4 Å) has an atomic radius more similar to Rh (1.3 Å), with In (1.6 Å) serving as an intermediate size. Additionally, each of the metals can form a 1:1 IMC with Rh. The crystalline phases of the synthesized materials are confirmed by powder X-ray diffraction (PXRD), Figure 1. Rh has a face-center cubic (fcc) structure, whereas RhGa and RhIn have a cubic CsCl-type structure. RhBi takes a hexagonal NiAs-type structure. The patterns for the as-synthesized RhM@MSWs match the corresponding calculated patterns in all cases. The crystallite size of the monometallic Rh nanoparticle is 3.6 nm, as calculated using Scherrer's equation and the collected PXRD pattern. Upon addition of the secondary metal, the crystalline size increases to 7-10 nm for all RhM iNPs from their PXRD patterns. The RhM iNPs have a larger than expected diameter for a single particle to single particle transformation, which indicates that Ostwald ripening and aggregation processes are involved during the conversion from Rh to RhM in TEG solution and high-temperature reduction.

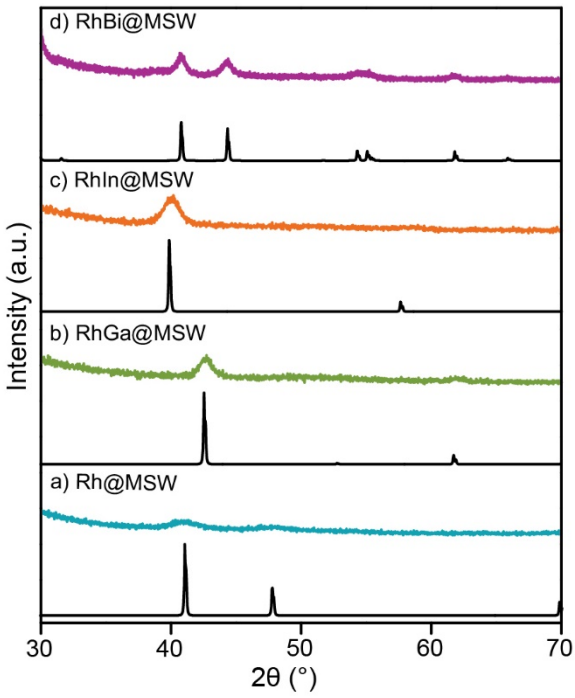

Figure 1. Structural characterization of RhM@MSWs. Powder X-ray diffraction patterns of a) Rh@MSW, b) RhGa@MSW, c) RhIn@MSW, and d) RhBi@MSW, with the respective standard patterns shown in black.

TEM studies were conducted to characterize the catalyst structure and the iNPs further. A few things can be learned from these TEM characterizations. First, the high-angle annular dark-field scanning transmission electron microscopy (HAADF-STEM) images confirm the morphology of the monometallic Rh@MSWs (Figure S3) and the RhM@MSWs iNPs (Figure 2a, 2c, and 2e). The mesoporous silica layer can be resolved and clearly distinguished from the solid silica core. Rh and RhM nanoparticles are well-dispersed between the mesoporous silica layer and the silica core, with an average particle of 3.7 ± 0.6 nm for Rh, 8.2 ± 1.3 nm for RhGa, 7.0 ± 1.3 nm for RhIn, and 9.3 ± 1.2 nm for RhBi. The average particle sizes are calculated by counting >200 particles (Figure S4-S7) and match those values obtained from PXRD peak width (Figure 1). In addition, the energy dispersive x-ray spectroscopy (EDS) maps (Figures 2a, 2c, and 2e) show the atomic distribution of the RhM@MSWs iNPs, confirming that the Rh and the secondary metal are distributed homogeneously with no monometallic particles or phase segregation observed, indicating all Rh NPs are converted to RhM iNPs. Lastly, atomic resolution HAADF-STEM images and EDS mapping images confirm the crystal structure of the iNPs, as shown in Figure 2b for RhIn, Figure 2d for RhGa, and Figure 2f for RhBi. The crystal structure observed from EDS maps at atomic resolution matches the RhIn(100), RhGa(110), and RhBi(110) planes, supporting the formation of the corresponding intermetallic phases. Measurement of the lattice spacing with a distance of 3.25 Å for RhIn, 3.03 Å for RhGa, and 5.65 Å for RhBi further confirmed the crystal structure and orientation. The net signal after background subtraction from EDS raw spectra (Figure S8-S11) is used in these elemental maps to ensure accuracy.

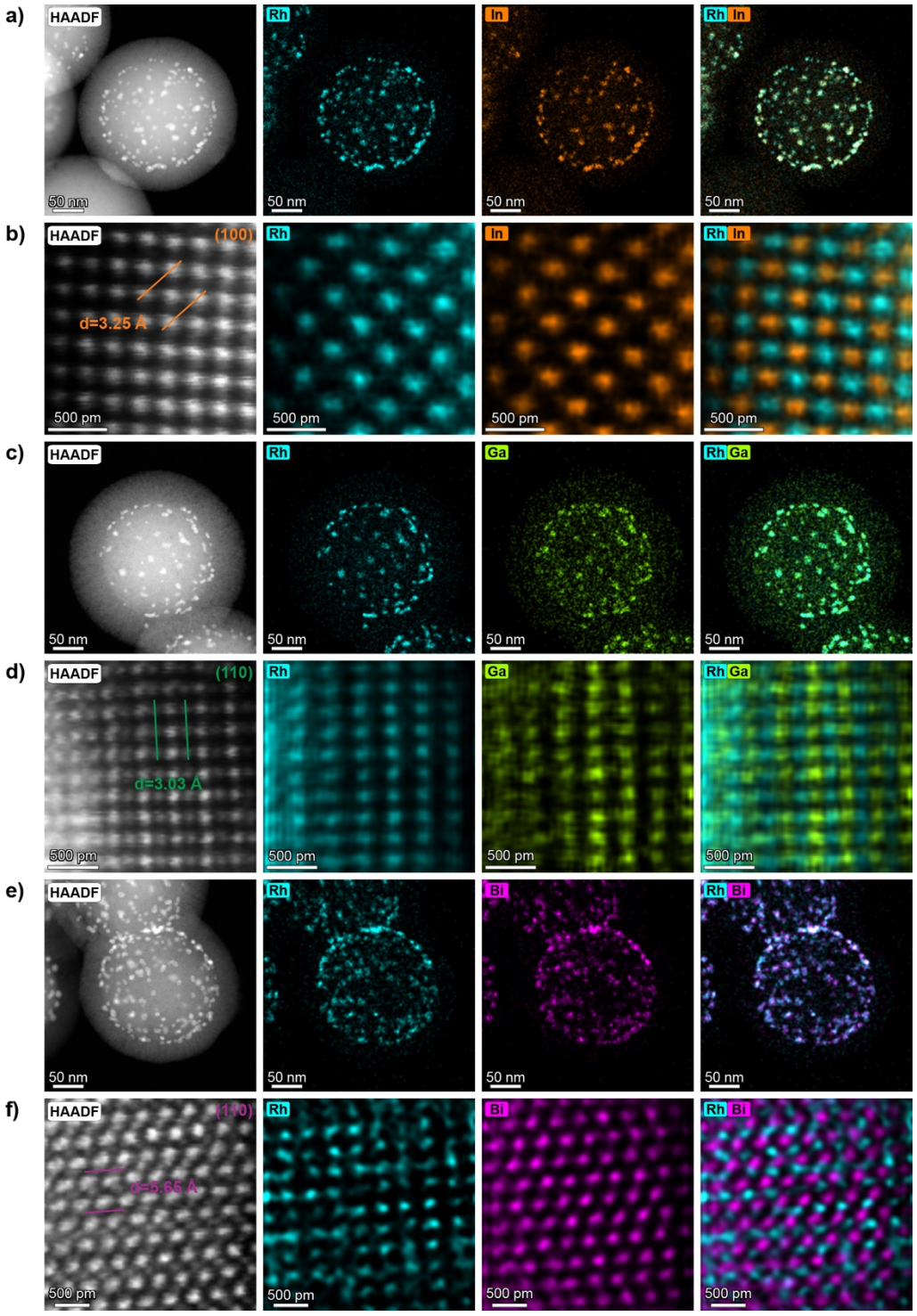

Figure 2. HAADF-STEM and EDS mapping images of a-b) RhIn@MSW, c-d) RhGa@MSW, and e-f) RhBi@MSW. A filter averaging three neighboring pixels has been applied to all EDS maps, and a radial Wiener filter has been applied to the atomic-resolution EDS maps to aid with the visualization.

N_2 physisorption measurements were performed for MSW, Rh@MSW, and RhM@MSW (Figure S12 and Table S1). All the materials show a Type IV isotherm, indicative of mesopores being present, as expected. The Brunauer-Emmett-Teller (BET) surface area of the starting, undecorated MSW is 439 m^2/g. The monometallic Rh@MSW has a surface area of 430 m^2/g, and the RhM@MSW BET surface areas range from 310-409 m^2/g. The trend in BET surface area is inversely related to the trend in nanoparticle size, indicating that the larger nanoparticles could be partially filling or blocking the mesopores. The Rh loading ranges from ~1.3-1.5 wt% according to the inductively coupled plasma mass spectrometry (ICP-MS) results in Table S2. The target stoichiometry for Rh: M_2 was 1:1 for all cases except for RhGa@MSW, which required excess Ga to form pure-phase RhGa iNPs.

2.2 Catalysis: Vapor-Phase Furfural Hydrogenation

The synthesized intermetallic catalysts were assessed for the vapor-phase hydrogenation of furfural using a plug flow reactor. As shown in Scheme 2, the furfural hydrogenation can take various pathways leading to many possible products. The complex reaction pathways can easily lead to a mixture of products, making achieving high selectivity challenging. Three possible reaction pathways for the hydrogenation of furfural are displayed in Scheme 2. Pathway I consists of the hydrogenation of the C=C bonds of the furan ring followed by the hydrogenation of the C=O carbonyl group to give tetrahydrofurfural and tetrahydrofurfuryl alcohol, respectively. Pathway II forms furfuryl alcohol (FOL) as an intermediate from the selective hydrogenation of the carbonyl group. Hydrogenolysis of C–O in FOL results in 2-methylfuran (2-MF) production. Pathway III starts with a decarbonylation step to form furan. Further hydrogenation and hydrogenolysis of the furan lead to butane as the primary product.

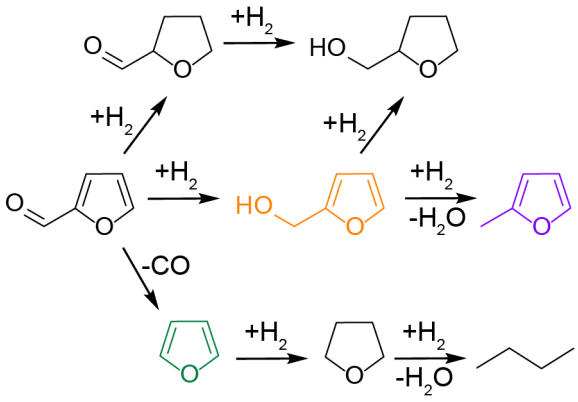

Scheme 2. Reaction pathways of furfural hydrogenation and decarbonylation.

A summary of product distribution is shown in Figure 3, with the conversion held at ~20% for all reactions except RhBi, which could only achieve ~2% conversion. The reported selectivity values are averaged from 3 trials with the standard deviation displayed in Figure S13. The turnover frequency (TOF) was calculated based on the amount of converted FAL and Rh dispersion obtained from CO chemisorption measurements of each catalyst (Figure 3). The calculated carbon balance (Table S3) reveals that approximately 100% of the input carbon is accounted for in each catalytic reaction. Monometallic Rh@MSWs yields various primary and secondary reaction products at 160 °C, with a majority (77%) being furan. FOL (1.9%) and 2-MF (6.2 %) are observed, along with a host of other products, including tetrahydrofuran (THF), butane, and tetrahydrofurfuryl alcohol (THFOL). The number and variety of products highlight the need for an improved catalyst design to enhance selectivity.

Adding a secondary metal to form iNPs resulted in different major products, as confirmed by GC-MS, being formed at the steady state for each metal combination. The intermetallic catalysts showed enhanced selectivity over the monometallic Rh@MSW. Adding Ga to form RhGa@MSW promoted furan selectivity to 89% by limiting further hydrogenation and hydrogenolysis to THF and butane and eliminating THFOL production. A decreased TOF is also noted, dropping from 81.5 h^{-1} for Rh@MSW to 24.4 h^{-1} for RhGa@MSW at 160 °C. For reference, Pd, a more typical decarbonylation catalyst, has achieved a TOF of 265.8 s^{-1} for the conversion of furfural to furan at 230 °C, 1 atm with an H_2:furfural feed ratio of 25.[24] RhIn@MSW-catalyzed furfural hydrogenation produced FOL with a selectivity of 97% and a TOF of 322.0 h^{-1}. The enhanced activity of RhIn@MSW compared to Rh@MSW could be attributed to the changed adsorption configuration and strength of furfural and furfuryl alcohol on the intermetallic surface,

similar to the observation on intermetallic PtSn.[34] Alloying Rh and Bi, on the other hand, resulted in a significantly lowered activity but with an enhanced selectivity to FOL (93%). The TOF for the RhBi could not be accurately calculated due to the weak CO adsorption, leading to inaccurate chemisorption results and Rh dispersion value. The catalyst-dependent selectivity was studied at high conversion and across different reaction temperatures (Figure S14). All the catalysts maintained the expected selectivity at higher conversions and only RhBi saw a decrease in selectivity as more furan was produced with increasing temperature. Additional experiments using the major product as the substrate for each catalyst (Table S4) showed that Rh@MSW is prone to overhydrogenation, explaining the lower selectivity for the monometallic catalyst. In contrast, the lack of significant conversion when using the RhM@MSWs further validates that the observed selectivity is intrinsic to the catalyst and not a function of specific reaction conditions. Metal-free MSWs and the monometallic secondary metals show no activity. Rh and RhM catalysts were also synthesized without a mesoporous silica shell (RhM/NH_2-SiO_2) and tested for the hydrogenation of furfural under the same reaction conditions used for the RhM@MSWs. The catalyst without a shell resulted in increased furfural conversion, exemplified by the RhIn/NH_2-SiO_2 TOF of 624.9 h^{-1} compared to the RhIn@MSW TOF of 322.0 h^{-1}. This increased activity indicates that the mesoporous shell blocks furfural from accessing some of the active sites. The product distribution shown in Figure S15 is nearly identical to the results reported for the RhM@MSWs (Figure 3) in all cases. The only exception is the Rh/NH_2-SiO_2, which produced more THF and butanes without the shell, but the selectivity to furan is similar. We attribute the changing chemoselectivity primarily to intermetallic-induced steric effects governed by the radius of the secondary metal. Electronic effects were disregarded as a significant factor because the trend in secondary metal electronegativity, and the resulting electron density of Rh, do not correlate well to the trend in catalytic behavior. These results demonstrate that the identity of the iNPs can be tuned to induce steric effects and control reaction selectivity.

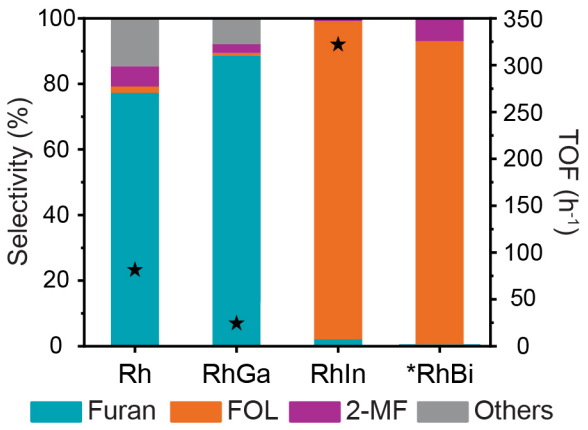

Figure 3. The quantitative product distribution of furfural hydrogenation using Rh@MSWs and RhM@MSWs (M = Ga, In, and Bi) catalysts, compared at ~20% conversion by adjusting the catalyst amount (Table S3). The catalysts were dispersed in 500 mg of quartz sand and packed into a U-shaped quartz reactor. Furfural = 0.3 μL/min, H_2 = 11.4 mL/min, He = 8.6 mL/min, 160 °C. *RhBi is only able to achieve approximately 2% conversion. The conversion-based TOF of each catalyst is designated by the star (★) symbol.

MSWs are designed to prevent particles from sintering at high temperatures and increase the catalyst stability and recyclability. For furfural hydrogenation, it is especially critical for the catalyst to be stable at high temperatures, as carbon deposition from furfural can lead to the catalyst deactivation.[23,39-41] A high-temperature oxidation and reduction treatment is necessary to regenerate the catalytic surface after this carbon deposition.[33,42] Therefore, to demonstrate the effectiveness of the mesoporous silica shell as a protective measure, the RhIn@MSW recyclability was explored and compared to a control catalyst without the porous silica shell, RhIn/NH_2-SiO_2. The catalysts were exposed to reaction conditions with the conversion tuned to approximately 50% by adjusting the amount of catalyst used. The catalysts were intentionally deactivated after 2 h by doubling the FAL flow (He= 17.2 mL/min) and adjusting the H_2 flow rate to 2.8 mL/min to maintain 20 mL/min total flow. The corresponding conversion and selectivity to furfuryl alcohol are displayed in Figure 4. Three deactivation-regeneration cycles were completed, with the RhIn@MSWs maintaining approximately 50% conversion and 95% FOL selectivity across all runs. Conversely, the RhIn/NH_2-SiO_2 experienced on-stream deactivation and was unable to recover the initial activity after the regeneration steps, dropping from 56 % conversion in the first cycle to 44 % in the third cycle. Additionally, the selectivity towards FOL decreased with each

cycle, indicating the deactivation-regeneration cycle impacted the structural properties of the RhIn NPs.

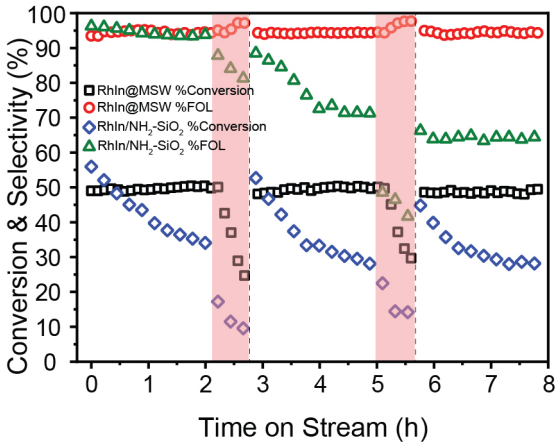

Figure 4. Furfural conversion and furfuryl alcohol selectivity during the recycling experiments using RhIn@MSW and RhIn/NH_2-SiO_2. The initial conversion was adjusted to approximately 50% by controlling the catalyst amount. The catalyst was dispersed in 500 mg of quartz sand and packed into a U-shaped quartz reactor. Initial conditions of furfural = 0.3 µL/min, H_2 = 11.4 mL/min, He = 8.6 mL/min, 160 °C were used. The catalysts were deactivated by flowing furfural = 0.6 µL/min, H_2 = 2.8 mL/min, He = 17.2 mL/min at 160 °C (shaded regions). The deactivated catalyst was calcined in air at 550 °C, 4 h, and reduced at 550 °C, 4 h, in 50 mL/min of 10% H_2/He. Three deactivation-regeneration cycles were performed, separated by the vertical dashed lines.

PXRD patterns of the RhIn@MSWs (Figure S16) catalyst look nearly identical before and after the regeneration cycles with a calculated particle size of 6.4 and 7.2 nm, respectively. Similarly, the collected TEM images (Figure S17) show very little change in the catalyst, with an average measured particle size of 7.0 ± 1.3 nm for the as-synthesized catalyst and 7.2 ± 1.4 nm after the recycling test (Figure S18). The same characterization was done for the RhIn/NH_2-SiO_2 with the PXRD (Figure S19) showing an increase in particle size from 11.4 to 13.0 nm. The average measured particle size from TEM (Figures S20-22) increases from 12.8 ± 4.1 to 15.4 ± 6.9 nm. It should be noted that the initial RhIn NPs without the protective shell are larger and have a broader size distribution than the fresh RhIn@MSW NPs, pointing to significant aggregation during the initial synthesis. The catalytic stability and material characterization demonstrate the effectiveness of the mesoporous silica wells at preventing NPs from aggregating during furfural hydrogenation and the corresponding catalyst regeneration steps.

2.3 DRIFTS Study

Diffuse reflectance infrared Fourier transform spectroscopy (DRIFTS) experiments were performed to study the surface of the catalysts using CO as a probe molecule (Figure 5). For monometallic Rh@MSW, a strong peak at 2068 cm^{-1} is observed, which is assigned to the atop adsorption of CO on Rh. The presence of bridged and geminal CO on Rh is detected as well. The bridged CO appears as a broad peak at 1917 cm^{-1}, with the geminal CO symmetric and asymmetric stretching at 2095 and 2024 cm^{-1}. Rh-based catalysts are rarely used in furfural hydrogenation but have been reported for the production of THFOL, FOL, and 1,5-pentanediol.[26,43-46] The formation of furan has only been reported using Rh(I) catalysts, whereas Rh(0) was inactive.[47] The geminal CO peaks indicate the presence of positively charged Rh species that could be the cause of the Rh selectivity to furan.[48–51] RhGa@MSW and RhIn@MSW show only the atop CO peak at 2036 and 2024 cm^{-1}, respectively. Performing the same CO DRIFTS experiment on RhBi@MSW results in a very weak linear CO peak at 2083 cm^{-1}. The lack of pronounced peaks indicates that CO interacts very weakly with RhBi iNPs, with only a small amount being adsorbed. The higher electronegativity of Rh compared to Ga and In results in more electron density on the alloyed Rh than the monometallic Rh and an enhanced electron back donation to the antibonding orbital of CO, lowering the frequency of the C≡O vibration.[52] Bi, on the other hand, is more electronegative than Rh, causing a more electropositive Rh upon alloying and a shift in the C≡O vibration to a higher wavenumber. The CO DRIFTS results highlight the difference between the monometallic and intermetallic surfaces, with CO showing multiple adsorption modes on pristine rhodium, only one type of adsorption on RhIn and RhGa, and a lack of adsorption in the RhBi case. The lack of the bridging CO peak (1917 cm^{-1}) indicates that the insertion of a secondary metal removed the typical bridge site on the Rh surface.

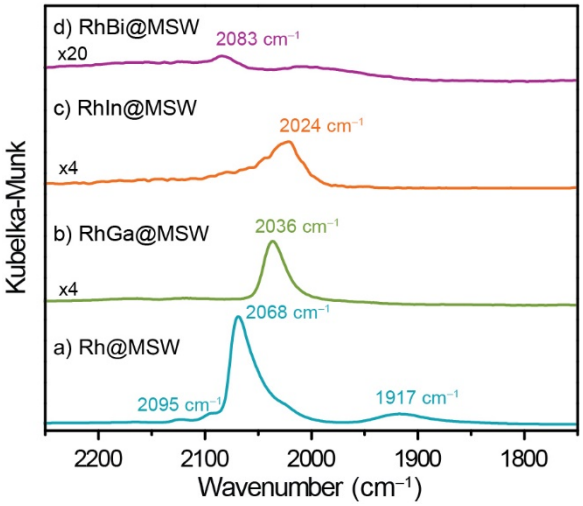

Figure 5. CO-DRIFTS studies for a) Rh@MSW, b) RhGa@MSW, c) RhIn@MSW, and d) RhBi@MSW recorded after flowing CO (20 mL/min) for 30 min and subsequent He (40 mL/min) flushing at 0°C.

The interactions of furfural with Rh, RhBi, RhGa, and RhIn under reaction conditions were investigated using FAL-DRIFTS (Figure 6) to provide insight into the relationship between the observed product selectivity and adsorption configuration. We first measured bare MSWs without Rh as a reference and observed no furfural adsorption on the SiO_2 support at 160 °C. Therefore, any peaks seen in the DRIFTS spectra of Rh@MSW and RhM@MSW are due to the adsorption of furfural or a reaction intermediate on the metal surface. For monometallic Rh@MSW, the characteristic carbonyl (1686 cm^{-1}) and furan ring (1581 and 1474 cm^{-1}) peaks are not observed.[53] Instead, two peaks at 2005 and 1851 cm^{-1} attributed to linear and bridging CO formed from the decarbonylation of furfural are observed. According to the metal-surface selection rule, the absence of carbonyl and furan ring peaks indicates the furfural adsorbs parallel to the Rh surface, as shown in Figure 8a.[54] For RhGa@MSW, a strong peak at 1628 cm^{-1} ascribed to the linear adsorption of the carbonyl group is observed, indicating that the aldehyde is bonded in the η_1(C) configuration with the C=O bond perpendicular to the surface. Weak furan ring peaks at 1566 and 1457 cm^{-1} suggest the furfural adsorbs in a tilted geometry that is nearly parallel to the RhGa surface (Figure 8a). Similar to the CO DRIFTS, these peaks are red-shifted due to the electron transfer from Ga to Rh. The high C=O/C=C peak intensity ratio (13.8) signifies a strong interaction between the furan ring and the metal surface, meaning the furfural is only slightly tilted away from the surface.[55] The RhIn results are very much the opposite. The carbonyl peak at 1630 cm^{-1} is

almost negligible, while the furan ring peaks are evident. This DRIFTS result indicates that the carbonyl is nearly parallel to the RhIn surface in the η_2(C,O) configuration, with the double bonds of the ring tilted away from the surface (Figure 8a). The C=O/C=C peak ratio (0.2) is much lower than the RhGa results, indicating that the ring is further tilted away from the surface and interacts less with the catalyst. Some linearly adsorbed CO is also observed for the RhGa (2004 cm^{-1}) and RhIn (1988 cm^{-1}). The production of CO on RhGa aligns well with the observed selectivity to the decarbonylation pathway but is somewhat unexpected for RhIn. Although some decarbonylation (2.1%) is observed on the RhIn, we propose the presence of an obvious CO peak during FAL-DRIFTS is primarily due to the strong adsorption of CO on RhIn resulting in CO accumulation. Additionally, the FAL-DRIFTS was done without the presence of hydrogen, meaning there is no hydrogenation pathway to compete with the decarbonylation pathway. The furfural DRIFTS of the largely inactive RhBi is similar to the RhIn case but with significantly weakened furan ring peaks and no observable free CO. This is due to the lack of furfural adsorption on RhBi (Figure 8a).

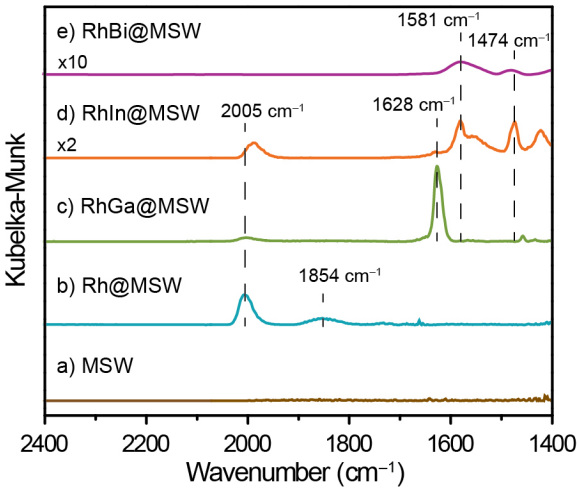

Figure 6. FAL-DRIFTS studies for a) MSW, b) Rh@MSW, c) RhGa@MSW, d) RhIn@MSW, and e) RhBi@MSW recorded after flowing furfural (0.3 μL/min) for 4 min and subsequent He (40 mL/min) flushing at 160°C.

The DRIFTS results correlate well with the observed catalytic results. The multiple CO adsorption modes and the parallel furfural adsorption on monometallic Rh explain the lower selectivity, as numerous products and pathways are possible based on the many plausible interactions with the active sites. For RhGa, very weak furan ring peaks indicate that the C=C bonds are slightly tilted further away from the active surface than in the Rh case. This adsorption

geometry leads to fewer possible reaction pathways within the furan ring and, thus, higher furan selectivity. It has also been reported that a higher furan selectivity is achievable through the η_1(C) configuration rather than the η_2(C,O) configuration observed on Rh.[60] The presence of only linear CO on RhIn shows effective active site isolation, preventing multiple reaction pathways from taking place at once. The furfural interacts with the RhIn in a tilted η_2(C,O) configuration, leading to the selective hydrogenation of the carbonyl rather than the double bonds of the furan ring. When testing RhBi, the furfural DRIFTS spectra show very weak peaks compared to the other iNPs. This indicates furfural is not efficiently adsorbed on the RhBi catalyst, correlating well to the observed lack of activity.

We attribute the observed behavior majorly to the surface steric effects of the iNPs. As the secondary metals' atomic radius increases, access to the Rh active sites becomes more restricted. This increased steric hindrance prevents the bulkier furan ring from lying flat on the surface, leading to the tilted configuration and a change in the reaction pathway, as is the case for RhIn. Ga, with an atomic radius closer to Rh, does not hinder access to the active site as much as In and thus follows the same reaction pathway as monometallic Rh. The increased selectivity towards furan is most likely due to the differences in how the carbonyl interacts with the Rh and the RhGa NPs. Alloying Rh with Bi introduces an even more significant atomic radius differential than the RhIn case, almost completely blocking the Rh sites, preventing furfural adsorption and conversion. Electronic effects were dismissed as the cause for product control as the trend in secondary metal electronegativity does not correlate well with the selectivity data.

2.4 DFT-based ML Accelerated Molecular Dynamics Studies

To reveal the surface structure of the iNPs, we performed molecular dynamics (MD) simulations using machine learning (ML) potentials derived from density-functional theory (DFT) calculations. To avoid bias towards a particular surface orientation, we simulated a randomly aggregated NP by sequentially adding Rh and Ga/In/Bi atoms with a fixed stoichiometry of 1:1, subject to a minimum distance requirement, and then equilibrated at 300 K for 10 ps after each addition. The resulting NP was then annealed from 300 K to 1600 K at various heating rates and then rapidly quenched back to 300 K. Figure 7 shows the real-space configurations of the Rh, RhGa, RhIn, and RhBi NPs obtained from the described procedures. For the Rh NP, regions of (111) and (100) surfaces are formed. For the RhGa NP, (100) and (110) facets are evident. For

RhIn, the surface is dominated by (100) facets. Conversely, the RhBi NP did not fully crystallize, even at the slowest simulated heating rate (20 K/ns). MD simulations of NPs formed from a Rh:M ratio of 2:1 were also performed to study the impact of atomic ratios on the particles' surfaces. The simulated results displayed in Figure S23 show that Ga, In, and Bi all prefer to be near the surface, as compared to Rh which occupies the interior of the particle. This tendency is the strongest for Bi and weakest for Ga. The propensity for Bi to be on the surface is such that the nanoparticle undergoes phase separation, forming a region with a pure Rh interior covered by a single layer of Bi and a Bi-rich intermetallic region.

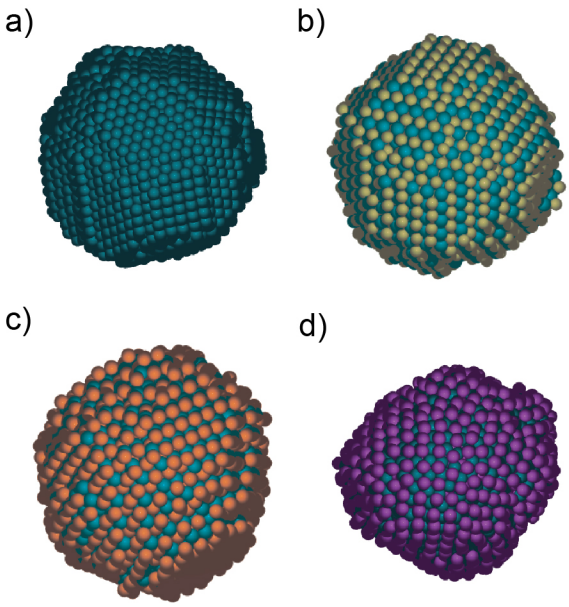

Figure 7. Molecular dynamics simulations for the formation of a) Rh, b) RhGa, c) RhIn, and d) RhBi nanoparticles.

We also performed machine learning accelerated molecular dynamics simulations to further study the interaction of furfural with each catalyst. First, we used the ML potentials for Rh, RhGa, RhIn, and RhBi to synthesize a slab of the respective metal or bimetallic system in a (1.9 × 1.9 × 3.8) nm^3 prismatic simulation cell with periodic boundary conditions at 1600 K. The slabs were then cooled down to 300 K at 1 K/ps. Furfural molecules were then added to the simulation cells containing the slabs sequentially at 300 K, subject to the condition that no atom was inserted

at a distance less than 2.8 Å away from the existing atoms, including both the metal and pre-existing furfural molecules. After each furfural molecule was inserted, the system was equilibrated with a short 1 ps ML MD run. Adsorption of furfural molecules on the Rh and RhM nanoparticles was also simulated using the ML potentials. Using a cubic simulation box of 9.6 nm in edge length with periodic boundary conditions, 256 furfural molecules are inserted into the simulation box sequentially within 16 ps at 300 K. The sample is then heated to 600 K at a heating rate of 1 K/ps. Figure S24 shows snapshots of the system at 600 K. For clarity, only furfural adsorbed on the NP are shown.

From ML simulations, we found that the furfural molecules adsorb on Rh, RhGa, and RhIn surfaces but not on the RhBi surface. Furfural molecules lie mostly flat on the Rh surface but are slightly tilted on RhGa and nearly completely vertical on RhIn, as shown in Figure 8a.

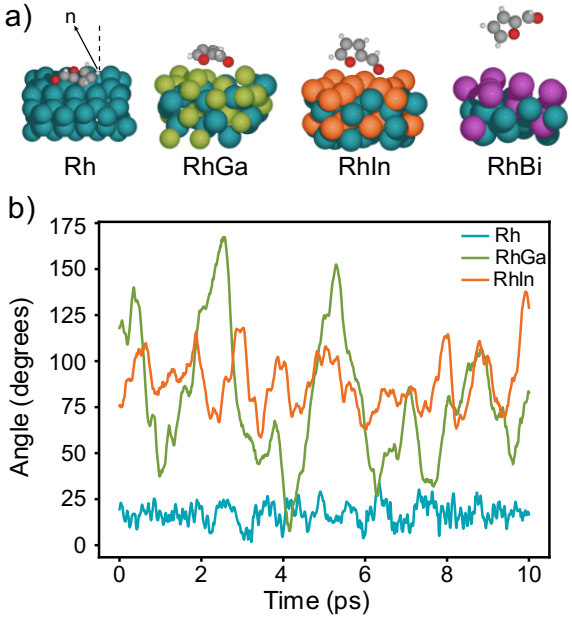

Figure 8. a) Illustration of furfural adsorption on Rh, RhGa, RhIn, and RhBi surface from machine learning potential simulations. Only a small portion of the simulation cell is shown. b) The angle between the normal vector of the furan ring and the normal of the metal surface as a function of time.

The differences between the adsorption of the furfural molecule on the RhGa and RhIn are more subtle. Figure 8b shows the angle between the normal vectors of the furan ring and the metal surface as a function of time for a single furfural molecule on Rh, RhGa, and RhIn. An angle near

0° or 180° means the molecule is flat, and an angle near 90° means the molecule is vertical. The simulations show that for the Rh surface, the furfural molecule lies flat during the entire 10 ps simulation at 300 K. On the RhGa surface, the molecule can rotate quite easily and be flat or vertical. On the RhIn surface, the furfural molecule remains mostly vertical throughout the simulation time frame. In general, the furfural molecules favored the edges between facets for Rh, RhGa, and RhIn. On RhBi, the furfural molecules only physisorb to the surface and maintain a high degree of mobility (Figure S24). Since there are no dominating facets for furfural adsorption, the effects of surface orientations can only be taken into account by a statistical analysis. However, the difference in furfural adsorption behavior due to the chemical composition of the nanoparticles is much more apparent than the simulations suggest. Our analysis shown in Figure 8, using a slab geometry with somewhat amorphous configurations, is representative. The simulated adsorption geometries and behavior agree well with the FAL DRIFTS results and provide further evidence for the proposed steric control of product selectivity.

3. Conclusion

In summary, by synthesizing and applying Rh-based intermetallic catalysts, we show that the identity of the secondary metal used to form iNPs can direct the selectivity of furfural hydrogenation. The secondary metal introduces surface steric effects that tune the furfural adsorption mode and enable product control. RhBi@MSW predominately resulted in blocked active sites and dramatically decreased interaction with furfural. Furan and furfuryl alcohol were selectively produced using RhGa@MSW and RhIn@MSW, respectively. The RhM@MSWs resulted in upwards of 85 % selectivity to the major product formed in each case. CO-DRIFTS studies contrasted the monometallic and intermetallic surfaces by confirming differing CO adsorption modes on the respective nanoparticles. FAL-DRIFTS studies, supported by DFT-based MD simulations, relate the reaction selectivity to the preferred adsorption configuration of furfural on the catalyst and, therefore, to the secondary metal size. During recycle and regeneration experiments, we demonstrate the enhanced stability of the iNPs confined between the solid silica core and the mesoporous silica shell. The steric effects detailed in this study provide a basis for further investigation into other iNP catalysts for selectively targeting products in catalytic reactions and increasing the efficiency and utility of biomass-derived chemical feedstocks.

4. ASSOCIATED CONTENT

4.1 Author Information

Charles J. Ward - Department of Chemistry, Iowa State University, Ames, IA 50011, United States; Ames National Laboratory, US Department of Energy, Ames, IA 50011, United States https://orcid.org/0000-0002-8040-9433

Minda Chen - Materials and Structural Analysis Division, Thermo Fisher Scientific, Hillsboro, OR, 97124, United States https://orcid.org/0000-0002-9881-9350

Andrew Lamkins - Department of Chemistry, Iowa State University, Ames, IA 50011, United States; Ames National Laboratory, US Department of Energy, Ames, IA 50011, United States

Claudio Ordonez - Department of Chemistry, Iowa State University, Ames, IA 50011, United States

Rong Sun - Department of Chemistry, Iowa State University, Ames, IA 50011, United States

Puranjan Chatterjee - Department of Chemistry, Iowa State University, Ames, IA 50011, United States; Ames National Laboratory, US Department of Energy, Ames, IA 50011, United States https://orcid.org/0000-0001-8107-4498

Minghui Niu - Department of Chemistry, Iowa State University, Ames, IA 50011, United States

Ruoyu Cui - Department of Chemistry, Iowa State University, Ames, IA 50011, United States

4.2 Corresponding Authors

Da-Jiang Liu Ames National Laboratory, US Department of Energy, Ames, IA 50011, United States. https://orcid.org/0000-0002-3019-9247

Wenyu Huang - Department of Chemistry, Iowa State University, Ames, IA 50011, United States; Ames National Laboratory, US Department of Energy, Ames, IA 50011, United States. https://orcid.org/0000-0003-2327-7259

4.3 Notes

The authors declare no conflict of interest.

4.4 Supporting Information

Synthesis and characterization methods, molecular dynamics simulations details, additional TEM, EDS, BET, and ICP characterization of the RhM@MSW catalysts, and XRD and TEM comparing the as-synthesized RhIn@MSW to the recycled RhIn@MSW.

4.5 ACKNOWLEDGEMENTS

This work is supported by NSF grant CHE-2108306/2108307 and the Trapp award from Iowa State University. The STEM/EDS experiment was performed at the Hillsboro Nanoport of Thermo Fisher Scientific by MC. The BET measurement by PC was supported by the U.S. Department of Energy (U.S. DOE), Office of Science, Basic Energy Sciences, Division of Chemical Sciences, Geosciences, and Biological Sciences, Separation Science Program. The DFT-aided ML accelerated MD studies performed by DJL were supported by the U.S. Department of Energy (U.S. DOE), Office of Science, Basic Energy Sciences, Division of Chemical Sciences, Geosciences, and Biological Sciences, Computational and Theoretical Chemistry (CTC) program. Research was performed at Ames National Laboratory, which is operated by Iowa State University under contract No. DE-AC02-07CH11358.

5. References

(1) Rößner, L.; Armbrüster, M. Electrochemical Energy Conversion on Intermetallic Compounds: A Review. *ACS Catal.* **2019**, *9* (3), 2018–2062, DOI: 10.1021/acscatal.8b04566.

(2) Yan, Y.; Du, J. S.; Gilroy, K. D.; Yang, D.; Xia, Y.; Zhang, H. Intermetallic Nanocrystals: Syntheses and Catalytic Applications. *Adv. Mater.* **2017**, *29* (14), 1605997, DOI: 10.1002/adma.201605997.

(3) Furukawa, S.; Komatsu, T. Intermetallic Compounds: Promising Inorganic Materials for Well-Structured and Electronically Modified Reaction Environments for Efficient Catalysis. *ACS Catal.* **2017**, *7* (1), 735–765, DOI: 10.1021/acscatal.6b02603.

(4) Marakatti, V. S.; Peter, S. C. Synthetically Tuned Electronic and Geometrical Properties of Intermetallic Compounds as Effective Heterogeneous Catalysts. *Prog. Solid. State Chem.* **2018**, *52*, 1–30, DOI: 10.1016/j.progsolidstchem.2018.09.001.

(5) Liu, J.; Lee, C.; Hu, Y.; Liang, Z.; Ji, R.; Soo, X. Y. D.; Zhu, Q.; Yan, Q. Recent Progress in Intermetallic Nanocrystals for Electrocatalysis: From Binary to Ternary to High-Entropy Intermetallics. *SmartMat* **2023**, *4* (4), e1210, DOI: 10.1002/smm2.1210.

(6) Prinz, J.; Gaspari, R.; Stöckl, Q. S.; Gille, P.; Armbrüster, M.; Brune, H.; Gröning, O.; Pignedoli, C. A.; Passerone, D.; Widmer, R. Ensemble Effect Evidenced by CO Adsorption on the 3-Fold PdGa Surfaces. *J. Phys. Chem. C* **2014**, *118* (23), 12260–12265, DOI: 10.1021/jp501584f.

(7) Liu, P.; Nørskov, J. K. Ligand and Ensemble Effects in Adsorption on Alloy Surfaces. *Phys. Chem. Chem. Phys.* **2001**, *3* (17), 3814–3818, DOI: 10.1039/B103525H.

(8) Furukawa, S.; Takahashi, K.; Komatsu, T. Well-Structured Bimetallic Surface Capable of Molecular Recognition for Chemoselective Nitroarene Hydrogenation. *Chem. Sci.* **2016**, *7* (7), 4476–4484, DOI: 10.1039/C6SC00817H.

(9) Miyazaki, M.; Furukawa, S.; Komatsu, T. Regio- and Chemoselective Hydrogenation of Dienes to Monoenes Governed by a Well-Structured Bimetallic Surface. *J. Am. Chem. Soc.* **2017**, *139* (50), 18231–18239, DOI: 10.1021/jacs.7b08792.

(10) Miller, I. J.; Fellows, S. K. Liquefaction of Biomass as a Source of Fuels or Chemicals. *Nature* **1981**, *289* (5796), 398–399. DOI: 10.1038/289398a0.

(11) Goyal, H. B.; Seal, D.; Saxena, R. C. Bio-Fuels from Thermochemical Conversion of Renewable Resources: A Review. *Renew. Sustain. Energy Rev.* **2008**, *12* (2), 504–517. DOI: 10.1016/j.rser.2006.07.014.

(12) Bruijnincx, P. C. A.; Weckhuysen, B. M. Lignin up for Break-Down. *Nat. Chem.* **2014**, *6* (12), 1035–1036. DOI: 10.1038/nchem.2120.

(13) Mathew, A. K.; Abraham, A.; Mallapureddy, K. K.; Sukumaran, R. K. Chapter 9 - Lignocellulosic Biorefinery Wastes, or Resources? In *Waste Biorefinery*; Bhaskar, T., Pandey, A., Mohan, S. V., Lee, D.-J., Khanal, S. K., Eds.; Elsevier, 2018; pp 267–297, DOI: 10.1016/B978-0-444-63992-9.00009-4.

(14) Jiménez-Gómez, C. P.; Cecilia, J. A.; García-Sancho, C.; Moreno-Tost, R.; Maireles-Torres, P. Selective Production of Furan from Gas-Phase Furfural Decarbonylation on Ni-MgO Catalysts. *ACS Sustainable Chem. Eng.* **2019**, *7* (8), 7676–7685, DOI: 10.1021/acssuschemeng.8b06155.

(15) Ozer, R. VAPOR PHASE DECARBONYLATION PROCESS. US 8,710,251 B2.

(16) Zhou, X.; Feng, Z.; Guo, W.; Liu, J.; Li, R.; Chen, R.; Huang, J. Hydrogenation and Hydrolysis of Furfural to Furfuryl Alcohol, Cyclopentanone, and Cyclopentanol with a Heterogeneous Copper Catalyst in Water. *Ind. Eng. Chem. Res.* **2019**, *58* (10), 3988–3993. DOI: 10.1021/acs.iecr.8b06217.

(17) Shi, Y.; Zhu, Y.; Yang, Y.; Li, Y.-W.; Jiao, H. Exploring Furfural Catalytic Conversion on Cu(111) from Computation. *ACS Catal.* **2015**, *5* (7), 4020–4032. DOI: 10.1021/acscatal.5b00303.

(18) Nakagawa, Y.; Nakazawa, H.; Watanabe, H.; Tomishige, K. Total Hydrogenation of Furfural over a Silica-Supported Nickel Catalyst Prepared by the Reduction of a Nickel Nitrate Precursor. *ChemCatChem* **2012**, *4* (11), 1791–1797. DOI: 10.1002/cctc.201200218.

(19) Liu, L.; Lou, H.; Chen, M. Selective Hydrogenation of Furfural to Tetrahydrofurfuryl Alcohol over Ni/CNTs and Bimetallic CuNi/CNTs Catalysts. *Int. J. of Hydrogen Energy* **2016**, *41* (33), 14721–14731. DOI: 10.1016/j.ijhydene.2016.05.188.

(20) Shao, Y.; Wu, J.; Zheng, Z.; Fan, M.; Sun, K.; Bkangmo Kontchouo, F. M.; Zhang, L.; Zhang, S.; Hu, G.; Hu, X. Alloying Cobalt in Co–Fe–Al Catalyst for Achieving the Selective Conversion of Furfural to Cyclopentanone. *Renew. Energy* **2022**, *195*, 957–971. DOI: 10.1016/j.renene.2022.06.068.

(21) Wang, G.-H.; Deng, X.; Gu, D.; Chen, K.; Tüysüz, H.; Spliethoff, B.; Bongard, H.-J.; Weidenthaler, C.; Schmidt, W.; Schüth, F. Co3O4 Nanoparticles Supported on Mesoporous Carbon for Selective Transfer Hydrogenation of α,β-Unsaturated Aldehydes. *Angew. Chem. Int. Ed.* **2016**, *128* (37), 11267–11271. DOI: 10.1002/anie.201604673.

(22) Ouyang, W.; Yepez, A.; Romero, A. A.; Luque, R. Towards Industrial Furfural Conversion: Selectivity and Stability of Palladium and Platinum Catalysts under Continuous Flow Regime. *Catal. Today* **2018**, *308*, 32–37. DOI: 10.1016/j.cattod.2017.07.011.

(23) Taylor, M. J.; Jiang, L.; Reichert, J.; Papageorgiou, A. C.; Beaumont, S. K.; Wilson, K.; Lee, A. F.; Barth, J. V.; Kyriakou, G. Catalytic Hydrogenation and Hydrodeoxygenation of Furfural over Pt(111): A Model System for the Rational Design and Operation of Practical Biomass Conversion Catalysts. *J. Phys. Chem. C* **2017**, *121* (15), 8490–8497. DOI: 10.1021/acs.jpcc.7b01744.

(24) Sitthisa, S.; Resasco, D. E. Hydrodeoxygenation of Furfural Over Supported Metal Catalysts: A Comparative Study of Cu, Pd and Ni. *Catal Lett* **2011**, *141* (6), 784–791. DOI: 10.1007/s10562-011-0581-7.

(25) Šivec, R.; Huš, M.; Likozar, B.; Grilc, M. Furfural Hydrogenation over Cu, Ni, Pd, Pt, Re, Rh and Ru Catalysts: Ab Initio Modelling of Adsorption, Desorption and Reaction Micro-Kinetics. *Chem. Eng. J.* **2022**, *436*, 135070. DOI: 10.1016/j.cej.2022.135070.

(26) Matsagar, B. M.; Hsu, C.-Y.; Chen, S. S.; Ahamad, T.; Alshehri, S. M.; Tsang, D. C. W.; Wu, K. C.-W. Selective Hydrogenation of Furfural to Tetrahydrofurfuryl Alcohol over a Rh-Loaded Carbon Catalyst in Aqueous Solution under Mild Conditions. *Sustainable Energy Fuels* **2020**, *4* (1), 293–301. DOI: 10.1039/C9SE00681H.

(27) MacIntosh, K. L.; Beaumont, S. K. Nickel-Catalysed Vapour-Phase Hydrogenation of Furfural, Insights into Reactivity and Deactivation. *Top Catal* **2020**, *63* (15), 1446–1462. DOI: 10.1007/s11244-020-01341-9.

(28) Kuhaudomlap, S.; Mekasuwandumrong, O.; Praserthdam, P.; Lee, K. M.; Jones, C. W.; Panpranot, J. Influence of Highly Stable Ni2+ Species in Ni Phyllosilicate Catalysts on Selective Hydrogenation of Furfural to Furfuryl Alcohol. *ACS Omega* **2023**, *8* (1), 249–261. DOI: 10.1021/acsomega.2c03590.

(29) Zhang, M.; Yang, J.-H. Selective Hydrogenation of Furfural: Pure Silica Supported Metal Catalysts. *ChemistrySelect* **2022**, *7* (9), e202200013. DOI: 10.1002/slct.202200013.

(30) Pushkarev, V. V.; Musselwhite, N.; An, K.; Alayoglu, S.; Somorjai, G. A. High Structure Sensitivity of Vapor-Phase Furfural Decarbonylation/Hydrogenation Reaction Network as a Function of Size and Shape of Pt Nanoparticles. *Nano Lett.* **2012**, *12* (10), 5196–5201. DOI: 10.1021/nl3023127.

(31) Taylor, M. J.; Durndell, L. J.; Isaacs, M. A.; Parlett, C. M. A.; Wilson, K.; Lee, A. F.; Kyriakou, G. Highly Selective Hydrogenation of Furfural over Supported Pt Nanoparticles under Mild Conditions. *Appl. Catal., B* **2016**, *180*, 580–585. DOI: 10.1016/j.apcatb.2015.07.006.

(32) Yan, K.; Chen, A. Selective Hydrogenation of Furfural and Levulinic Acid to Biofuels on the Ecofriendly Cu–Fe Catalyst. *Fuel* **2014**, *115*, 101–108. DOI: 10.1016/j.fuel.2013.06.042.

(33) Fang, R.; Liu, H.; Luque, R.; Li, Y. Efficient and Selective Hydrogenation of Biomass-Derived Furfural to Cyclopentanone Using Ru Catalysts. *Green Chem.* **2015**, *17* (8), 4183–4188. DOI: 10.1039/C5GC01462J.

(34) Maligal-Ganesh, R. V.; Xiao, C.; Goh, T. W.; Wang, L.-L.; Gustafson, J.; Pei, Y.; Qi, Z.; Johnson, D. D.; Zhang, S.; Tao, F. (Feng); Huang, W. A Ship-in-a-Bottle Strategy To Synthesize Encapsulated Intermetallic Nanoparticle Catalysts: Exemplified for Furfural Hydrogenation. *ACS Catal.* **2016**, *6* (3), 1754–1763, DOI: 10.1021/acscatal.5b02281.

(35) Yang, Y.; Chen, L.; Chen, Y.; Liu, W.; Feng, H.; Wang, B.; Zhang, X.; Wei, M. The Selective Hydrogenation of Furfural over Intermetallic Compounds with Outstanding Catalytic Performance. *Green Chem.* **2019**, *21* (19), 5352–5362, DOI: 10.1039/C9GC01119F.

(36) Maligal-Ganesh, R. V.; Pei, Y.; Xiao, C.; Chen, M.; Goh, T. W.; Sun, W.; Wu, J.; Huang, W. Sub-5 Nm Intermetallic Nanoparticles Confined in Mesoporous Silica Wells for Selective

Hydrogenation of Acetylene to Ethylene. *ChemCatChem* **2020**, *12* (11), 3022–3029, DOI: 10.1002/cctc.202000155.

(37) Dong, B.; Pei, Y.; Zhao, F.; Goh, T. W.; Qi, Z.; Xiao, C.; Chen, K.; Huang, W.; Fang, N. In Situ Quantitative Single-Molecule Study of Dynamic Catalytic Processes in Nanoconfinement. *Nat Catal* **2018**, *1* (2), 135–140, DOI: 10.1038/s41929-017-0021-1.

(38) Xiao, C.; Maligal-Ganesh, R. V.; Li, T.; Qi, Z.; Guo, Z.; Brashler, K. T.; Goes, S.; Li, X.; Goh, T. W.; Winans, R. E.; Huang, W. High-Temperature-Stable and Regenerable Catalysts: Platinum Nanoparticles in Aligned Mesoporous Silica Wells. *ChemSusChem* **2013**, *6* (10), 1915–1922, DOI: 10.1002/cssc.201300524.

(39) Rao, R.; Dandekar, A.; Baker, R. T. K.; Vannice, M. A. Properties of Copper Chromite Catalysts in Hydrogenation Reactions. *J. Catal.* **1997**, *171* (2), 406–419. DOI: 10.1006/jcat.1997.1832.

(40) Liu, D.; Zemlyanov, D.; Wu, T.; Lobo-Lapidus, R. J.; Dumesic, J. A.; Miller, J. T.; Marshall, C. L. Deactivation Mechanistic Studies of Copper Chromite Catalyst for Selective Hydrogenation of 2-Furfuraldehyde. *J. Catal.* **2013**, *299*, 336–345. DOI: 10.1016/j.jcat.2012.10.026.

(41) Kalong, M.; Hongmanorom, P.; Ratchahat, S.; Koo-amornpattana, W.; Faungnawakij, K.; Assabumrungrat, S.; Srifa, A.; Kawi, S. Hydrogen-Free Hydrogenation of Furfural to Furfuryl Alcohol and 2-Methylfuran over Ni and Co-Promoted Cu/γ-Al2O3 Catalysts. *Fuel Process. Technol.* **2021**, *214*, 106721. DOI: 10.1016/j.fuproc.2020.106721.

(42) Panagiotopoulou, P.; Martin, N.; Vlachos, D. G. Liquid-Phase Catalytic Transfer Hydrogenation of Furfural over Homogeneous Lewis Acid–Ru/C Catalysts. *ChemSusChem* **2015**, *8* (12), 2046–2054. DOI: 10.1002/cssc.201500212.

(43) Neeli, C. K. P.; Chung, Y.-M.; Ahn, W.-S. Catalytic Transfer Hydrogenation of Furfural to Furfuryl Alcohol by Using Ultrasmall Rh Nanoparticles Embedded on Diamine-Functionalized KIT-6. *ChemCatChem* **2017**, *9* (24), 4570–4579. DOI: 10.1002/cctc.201701037.

(44) Castelbou, J. L.; Szeto, K. C.; Barakat, W.; Merle, N.; Godard, C.; Taoufik, M.; Claver, C. A New Approach for the Preparation of Well-Defined Rh and Pt Nanoparticles Stabilized by Phosphine-Functionalized Silica for Selective Hydrogenation Reactions. *Chem. Commun.* **2017**, *53* (22), 3261–3264. DOI: 10.1039/C6CC10338C.

(45) Liu, S.; Amada, Y.; Tamura, M.; Nakagawa, Y.; Tomishige, K. Performance and Characterization of Rhenium-Modified Rh–Ir Alloy Catalyst for One-Pot Conversion of Furfural into 1,5-Pentanediol. *Catal. Sci. Technol.* **2014**, *4* (8), 2535–2549. DOI: 10.1039/C4CY00161C.

(46) Pisal, D. S.; Yadav, G. D. Single-Step Hydrogenolysis of Furfural to 1,2-Pentanediol Using a Bifunctional Rh/OMS-2 Catalyst. *ACS Omega* **2019**, *4* (1), 1201–1214. DOI: 10.1021/acsomega.8b01595.

(47) Lejemble, P.; Gaset, A.; Kalck, P. From Biomass to Furan through Decarbonylation of Furfural under Mild Conditions. *Biomass* **1984**, *4* (4), 263–274. DOI: 10.1016/0144-4565(84)90039-8.

(48) Zhu, H.; Li, Y.; Zheng, X. In-Situ DRIFTS Study of CeO2 Supported Rh Catalysts for N2O Decomposition. *Appl. Catal. A Gen.* **2019**, *571*, 89–95. DOI: 10.1016/j.apcata.2018.12.020.

(49) Varga, E.; Pusztai, P.; Óvári, L.; Oszkó, A.; Erdőhelyi, A.; Papp, C.; Steinrück, H.-P.; Kónya, Z.; Kiss, J. Probing the Interaction of Rh, Co and Bimetallic Rh–Co Nanoparticles with the CeO2 Support: Catalytic Materials for Alternative Energy Generation. *Phys. Chem. Chem. Phys.* **2015**, *17* (40), 27154–27166. DOI: 10.1039/C5CP03549J.

(50) Marino, S.; Wei, L.; Cortes-Reyes, M.; Cheng, Y.; Laing, P.; Cavataio, G.; Paolucci, C.; Epling, W. Rhodium Catalyst Structural Changes during, and Their Impacts on the Kinetics of, CO Oxidation. *JACS Au* **2023**, *3* (2), 459–467. DOI: 10.1021/jacsau.2c00595.

(51) Chen, M.; Gupta, G.; Ordonez, C. W.; Lamkins, A. R.; Ward, C. J.; Abolafia, C. A.; Zhang, B.; Roling, L. T.; Huang, W. Intermetallic Nanocatalyst for Highly Active Heterogeneous Hydroformylation. *J. Am. Chem. Soc.* **2021**, *143* (49), 20907–20915. DOI: 10.1021/jacs.1c09665.

(52) Bistoni, G.; Rampino, S.; Scafuri, N.; Ciancaleoni, G.; Zuccaccia, D.; Belpassi, L.; Tarantelli, F. How π Back-Donation Quantitatively Controls the CO Stretching Response in Classical and Non-Classical Metal Carbonyl Complexes. *Chem. Sci.* **2016**, *7* (2), 1174–1184. DOI: 10.1039/C5SC02971F.

(53) Meng, X.; Yang, Y.; Chen, L.; Xu, M.; Zhang, X.; Wei, M. A Control over Hydrogenation Selectivity of Furfural via Tuning Exposed Facet of Ni Catalysts. *ACS Catal.* **2019**, *9* (5), 4226–4235. DOI: 10.1021/acscatal.9b00238.

(54) Greenler, R. G.; Snider, D. R.; Witt, D.; Sorbello, R. S. The Metal-Surface Selection Rule for Infrared Spectra of Molecules Adsorbed on Small Metal Particles. *Surf. Sci.* **1982**, *118* (3), 415–428. DOI: 10.1016/0039-6028(82)90197-2.

(55) Yu, W.; Xiong, K.; Ji, N.; Porosoff, M. D.; Chen, J. G. Theoretical and Experimental Studies of the Adsorption Geometry and Reaction Pathways of Furfural over FeNi Bimetallic Model Surfaces and Supported Catalysts. *J. Catal.* **2014**, *317*, 253–262. DOI: 10.1016/j.jcat.2014.06.025.

(56) Zhang, W.; Zhu, Y.; Niu, S.; Li, Y. A Study of Furfural Decarbonylation on K-Doped Pd/Al2O3 Catalysts. *J. M. Catal. A Chem.* **2011**, *335* (1), 71–81. DOI: 10.1016/j.molcata.2010.11.016.